

Article

Influence of Tungsten Addition on Microstructure and Tensile Properties of Ti6Al4V Fabricated by Laser-Directed Energy Deposition

Junguo Li ¹ , Jinding Xiong ¹ , Yi Sun ^{1,2,*} and Qinqin Wei ¹

¹ State Key Laboratory of Advanced Technology for Materials Synthesis and Processing, Wuhan University of Technology, Wuhan 430070, China; lijg000@126.com (J.L.); xiongjd@foxmail.com (J.X.)

² Hubei Longzhong Laboratory, Xiangyang 441000, China

* Correspondence: sunyiwhut@163.com; Tel.: +86-187-7102-1416

Abstract: The addition of tungsten can improve the high-temperature oxidation resistance of titanium alloys. However, as its applications continue to expand, new demands are being placed on its room temperature strength. Here, we provide a dense titanium alloy with high strength by introducing proper W powders into the Ti6Al4V powders under direct energy deposition. The effect of tungsten addition on the microstructure and tensile properties of the Ti6Al4V alloy was investigated. Compared to pure Ti6Al4V, the titanium alloy with tungsten addition exhibited refined α' martensite and β grains, which is attributable to the effect of tungsten on the structural subcooling of titanium and on the formation temperature of the α' martensite. Owing to the synergistic strengthening effects of grain refinement and solid solution strengthening, the W-containing alloy shows a high tensile strength of 1333 MPa and yield strength of 1219 MPa, which are significantly higher than Ti6Al4V alloy's tensile strength of 940 MPa and yield strength of 860 MPa. This approach provides a pathway for design and preparation of high-strength titanium alloys by additive manufacturing.

Keywords: direct energy deposition; Ti6Al4V; microstructure; mechanical properties; grain refinement



Citation: Li, J.; Xiong, J.; Sun, Y.; Wei, Q. Influence of Tungsten Addition on Microstructure and Tensile Properties of Ti6Al4V Fabricated by Laser-Directed Energy Deposition. *Metals* **2023**, *13*, 1064. <https://doi.org/10.3390/met13061064>

Academic Editors: Vera Popovich, Thorsten Becker and Thomas Gries

Received: 28 April 2023

Revised: 29 May 2023

Accepted: 31 May 2023

Published: 1 June 2023



Copyright: © 2023 by the authors. Licensee MDPI, Basel, Switzerland. This article is an open access article distributed under the terms and conditions of the Creative Commons Attribution (CC BY) license (<https://creativecommons.org/licenses/by/4.0/>).

1. Introduction

Ti6Al4V, the most widely used titanium alloy, is composed of α and β dual-phase. For additive-manufactured titanium alloys, there are two common methods for controlling microstructure and properties. One is to adjust process parameters such as laser power, spot size, scanning speed, scanning method, etc. [1–8]. Another method is to add other alloying elements in titanium alloys to change the grain size, morphology, distribution, and content of α and β phases or generate new compounds to strengthen the matrix [9–15].

The addition of alloy elements changes the growth limitation factor Q , which corresponds to the development rate of structural undercooling relative to the development rate of solids [16]. The elements with larger Q values play a strong partitioning role at the solid–liquid solidification front, resulting in strong structural subcooling, which further promotes nucleation and eventually leads to grain refinement.

Bermingham et al. [15] significantly refined the size of primary β grains and reduced the length of α slats by adding Be, the element with the most significant theoretical effect on Ti refinement, i.e., the relatively largest Q value, to cast CP-Ti. Moreover, a comparison with other grain-refining elements pointed out that the refining effect of different elements in Ti on grains can be added independently. Xue et al. [12] added a trace amount of B to Ti6Al4V to refine the grains by the larger Q value of B on the one hand, and on the other hand, the in situ generated TiB was distributed among the grains so that the β and α crystals were reduced in size and equiaxed. Mendoza et al. [14] studied the grain refinement effect

of tungsten in titanium-based alloys and its related mechanism and pointed out that the Easton and St. John model is very suitable for the Ti-W system.

It has been reported that tungsten (W) has been widely used in high-temperature titanium alloys [17,18] due to its high melting point and its role in improving high-temperature strength and oxidation resistance. Among the alloying elements of titanium that do not form intermetallic compounds with titanium, tungsten ($Q \approx 22C0$), which has the most obvious elemental refinement effect, has been neglected and there is a lack of studies on the effect of tungsten on the mechanical properties of titanium alloys. Therefore, we investigated the mechanism of diffusion and grain refinement of tungsten on titanium alloy and the mechanism of mechanical properties by adding the W element to Ti6Al4V prepared by additive manufacturing. Therefore, it provides a new idea for alloying in titanium alloys for additive manufacturing.

2. Materials and Methods

2.1. Deposition Process and Processing Conditions

Titanium alloys with different W content (0, 3, 6, 9, and 12 at%, denoted as S0, S1, S2, S3, and S4, respectively) were prepared by DED equipment with three-axis environmental chamber and integrated Raycus single-module continuous laser under argon atmosphere with oxygen content below 50 ppm and the track filled in the direction of 45° .

W and Ti6Al4V spherical powders with a particle size of 45–105 μm were mechanically mixed, then dried in a vacuum oven at 120°C for 4 h. During deposition, the power was 400 W, the line speed was 10 mm/s, the spot diameter was 1.0 mm, and the powder feed rate was 1 r/min (1 g/min). The deposited samples had a size of 20 mm \times 20 mm \times 10 mm.

2.2. Microstructural Characterization and Mechanical Test

Sheet samples were cut longitudinally along the specimen for metallographic observation and compositional analysis. Compositional analysis was carried out using a Rigaku Ultima III X-ray diffractometer (XRD). Microstructure and chemical compositions were measured by metallographic observation on samples etched with Kroll reagent (1 mL HF, 3 mL HNO₃, and 50 mL H₂O) for 20 s after polishing and rinsing with alcohol, and a scanning electron microscope (SEM, Zeiss Gemini300) equipped with energy dispersive X-ray spectrometer (EDS), and a transmission electron microscope (TEM, FEI Talos F200X G2). Samples for TEM tests were prepared with a Focused Ion Beam Scanning Electron Microscope (FIB, FEI Scios 2 HiVac) and the samples were cut from the longitudinal section along the titanium alloys. Micro-tensile experiments were tested by a universal testing machine (INSTRON 5966) under a strain rate of 0.3 mm/min with an extensometer, and the tensile direction of the specimen was perpendicular to the direction of construction. The dimensions of the tensile specimen are shown in Figure 1e.

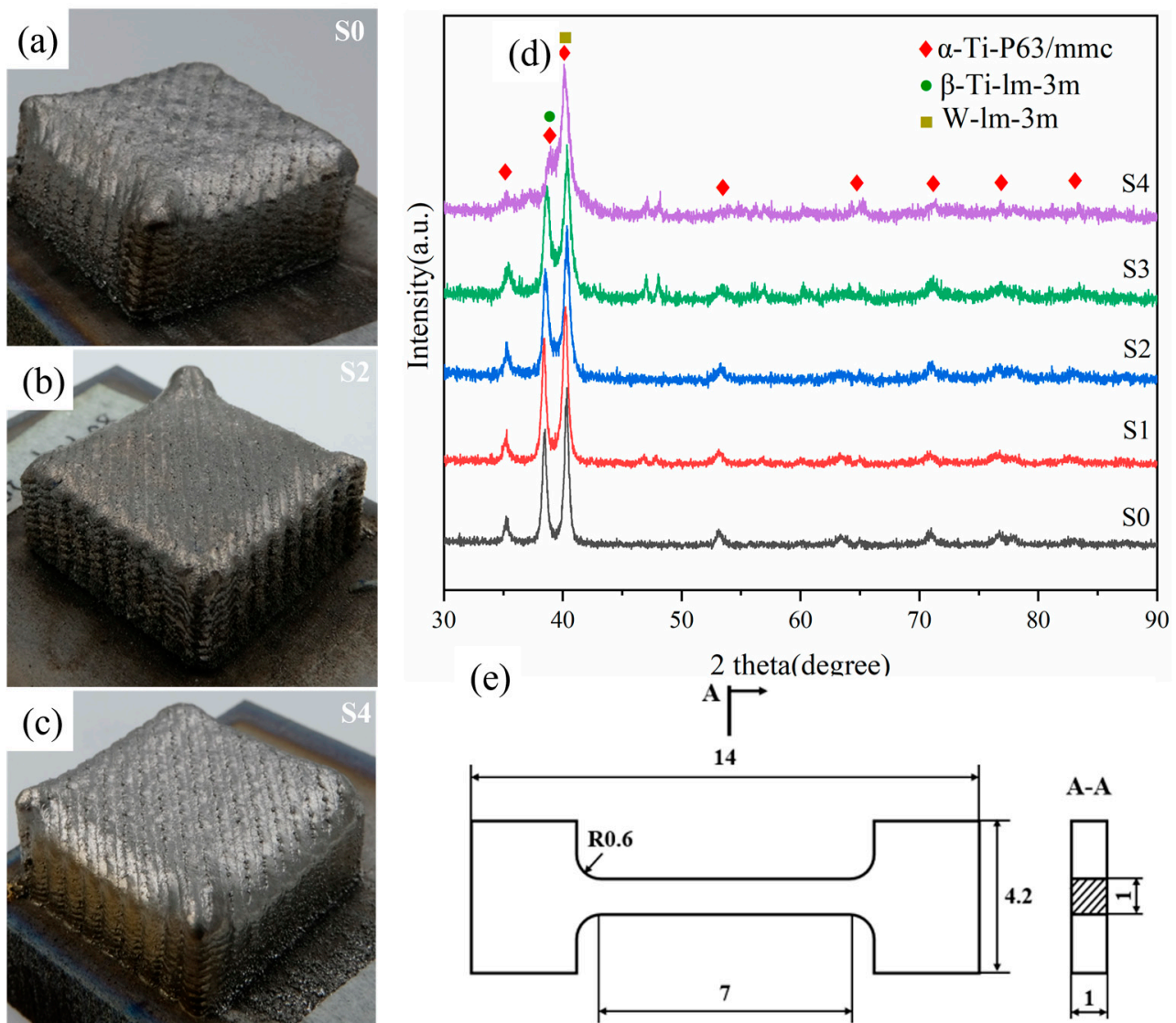


Figure 1. (a–c) Macroscopic pictures of the S0, S2, and S4 alloys; (d) XRD patterns of Ti6Al4V alloys with different W content; (e) Schematic diagram of micro-tensile specimen size (Numbers are in millimeters).

3. Results

3.1. As-Deposited Sample

Figure 1a–c shows the macroscopic pictures of the titanium alloys. The Ti6Al4V-W samples were successfully fabricated using the DED technique. The surface of the samples is relatively rough, and the cladding track is obvious. Some spherical particles are observed on the outer surface, which is the balling phenomenon caused by the flow driven by the surface tension gradient in the molten pool near the outer surface of the sample [19]. Deposited parts are tightly bonded to the substrate and no visible cracks are observed.

3.2. As-Deposited Microstructure

Figure 1d shows the XRD patterns of the Ti6Al4V-W alloy. For the Ti6Al4V alloy, all peaks coincide with α and β . As the added W content increases, the peaks of the tungsten–titanium solid solution and the β phase overlapping with the peaks of the α phase can be detected. However, since the peaks of the tungsten–titanium solid solution and the β phase overlap with the peaks of the α phase, and the atomic radius of tungsten

is similar to that of titanium, the formed substitutional solid solution has little effect on the interplanar spacing, and thus the existence of the β phase and the solid solution phase cannot be separately identified by the XRD spectrum.

Figure 2a–f shows the metallographic image of the longitudinal cross section of Ti6Al4V-W. Without the addition of W, prior β grains growing in a selective orientation along the construction direction across several cladding layers are visible. When the laser is swept from one direction to another, the resulting melt pool is hemisphere-like in shape, and the first generated β grains grow in the direction of the largest temperature gradient (Figure 2g) which is perpendicular to the edge of the melt pool, which is at the same time at an acute angle to the scanning direction. The newly generated β grains repeat the process while the angle is along the construction direction and at an acute angle to the laser direction, generating β grains that span several layers and are generally serrated upward.

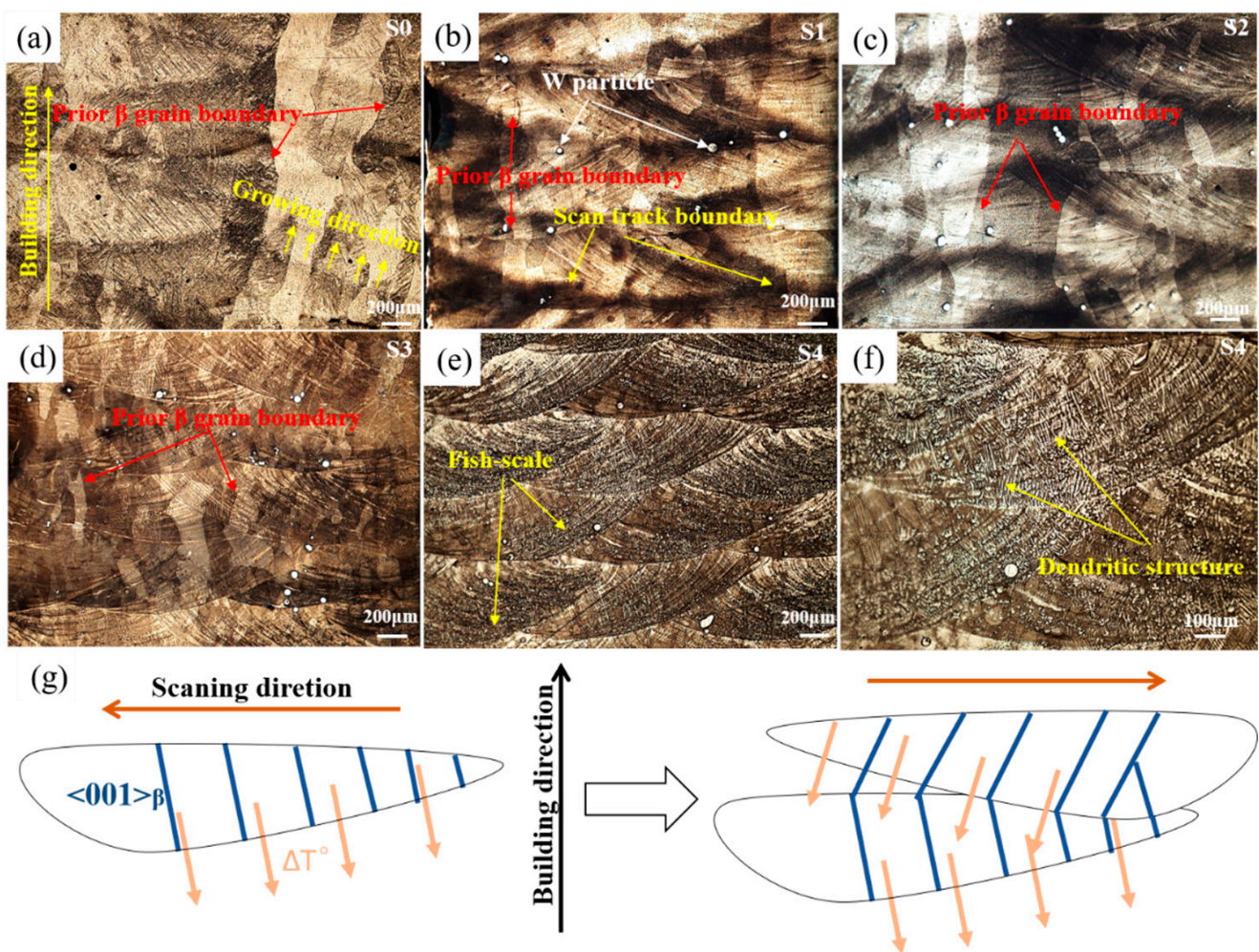


Figure 2. Longitudinal sections of the metallographic image under optical microscope of Ti6Al4V-W deposits: (a–e) S0–S4, respectively, (f) enlarged view of (e), (g) the growth schematic diagram of the prior β grains.

The S1 to S3 samples are all very similar in structure, consisting of prior β grains extending along the construction direction and fine needle-like α' martensite in the β grains. With the addition of W, the boundary of the melt pool gradually becomes clear, producing fish scale-like corrosion marks, and the tungsten particles are more distributed at the bottom of the melt pool. This may be due to the agglomeration of tungsten particles making less W at the edge of the melt pool [14], in addition to the lower temperature at the edge of the melt pool allowing less tungsten to bond with titanium to form a solid

solution. This allows each area to be corroded to different depths by producing different electronegativities in the primary cell reaction that occurs during corrosion. The initial β grains were significantly refined with increasing W content, and a trend of equiaxialization was observed. The previous β -grain boundaries of the S4 sample were hardly observed, while the dendritic structure was more obvious.

The deposited alloys show dense microstructure with fewer pores and cracks and no intermetallic compounds, while some tungsten particles are distributed and tightly bound in the matrix (Figure 3a). The melting point of tungsten is higher than the boiling point of titanium, and it is difficult to melt and fully alloy tungsten and titanium simultaneously under the same laser heat source. Figure 3b–o shows backscattered electron micrographs (BSE) for Ti6Al4V-W deposits and their higher magnification image. With the amount of added tungsten increasing, the lining of the melt pool generated during the printing process becomes obvious and the edges of the melt pool are darker than the center, thus forming a fish scale pattern (Figure 3b–e). In addition, with the increased addition of W (Figure 3f–j), a long dendrite-like structure with only one dendrite gradually appears in the melt pool and the dendrite length gradually becomes shorter or even partially equiaxed as the amount of added tungsten rises. The complex flow environment of the melt pool makes compositional undulations more common, and according to the tungsten–titanium phase diagram (Figure 4c), the high W content produces more structural subcooling. The cooling rate of the melt pool in additive manufacturing is very fast, resulting in dendritic segregation. Because the maximum temperature gradient is perpendicular to the edge of the melt pool downward, the dendrites grow in the direction of the maximum temperature gradient. This, coupled with the extremely fast cooling rate of the melt pool, makes it difficult to produce secondary dendrites. The difference in tungsten content in the dendrites and dendrite spacing results in black and white dendrite streaks in the BSE. As the W content increases, the compositional ups and downs of solutes become more common, nucleation and crystallization are easier, so the corresponding dendrites become shorter. This phenomenon and conclusion coincide with the simulation results of Rolchigo et al. [20]. Correspondingly, the β grains in Figure 2a–d gradually refine with the addition of tungsten as well as equiaxial.

By enlarging the bright and dark stripes in Figure 3f–j, a series of microstructure diagrams can be obtained as in Figure 3k–o, showing the morphology and distribution changes of α' martensite. Ti6Al4V is a relatively classical $\alpha+\beta$ duplex titanium alloy, which undergoes $\beta\rightarrow\alpha$ transformation under slow cooling conditions, and after the cooling rate exceeds about 525 °C/s only $\beta\rightarrow\alpha'$ transformation occurs to generate α' martensite [21]. The cooling rate of DED (about 7×10^4 K/s) [22] greatly exceeds the critical cooling rate, thus only α' martensite is produced. With the addition of tungsten, as shown in Figure 3k–o, it can be observed that the α' martensite is significantly refined, and submicron α' martensite is already present in the S1 sample, while the refinement is most obvious in the S3 sample, where most of the α' martensite is in submicron structure. In addition, it can be observed that the α' martensite in the white area is significantly more refined than that in the black area. We performed an EDS-line scan on the light and dark stripes of the S3 sample, as shown in Figure 3n, which shows that the tungsten content is more at the white stripes and less at the black stripes. It also shows that tungsten has a more obvious refining effect on α' martensite. Because tungsten is a β phase stabilizing element, the α' martensite gradually disappears after the content of tungsten rises to a certain degree, while the β phase gradually increases (Figure 3o). The number of martensites in the S4 sample decreases to unobservable, while the content of β phase increases.

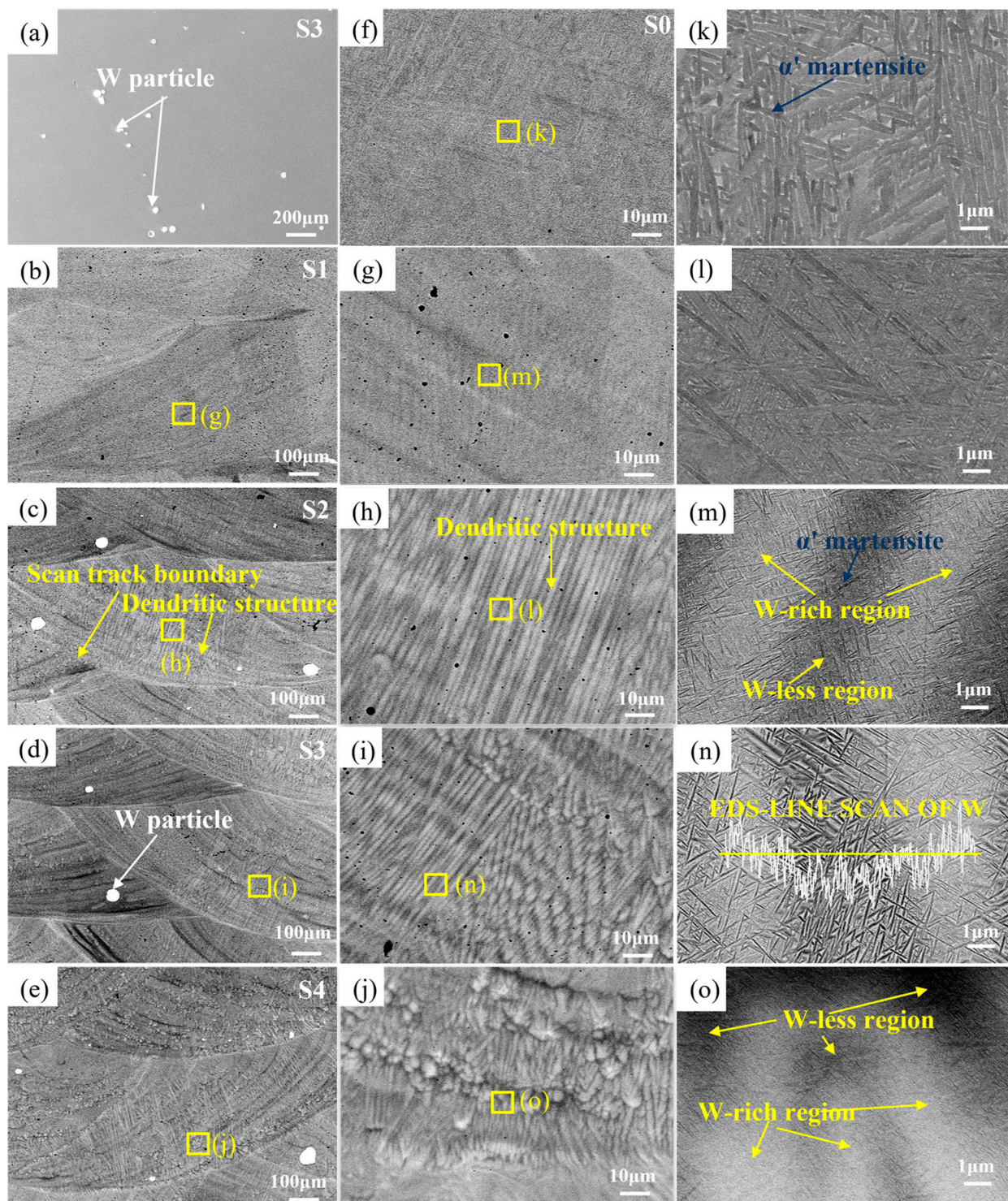


Figure 3. (a) SEM of S3 alloys; Backscattered electron micrographs for Ti6Al4V-W deposits and their higher magnification image: (f,k) are the S0, (b,g,m) are the S1, (c,h,l) are the S2, (d,i,n) are the S3, and (e,j,o) are the S4, where (n) is the EDS line scan of the bright and dark stripes of W elements in the S3 alloy.

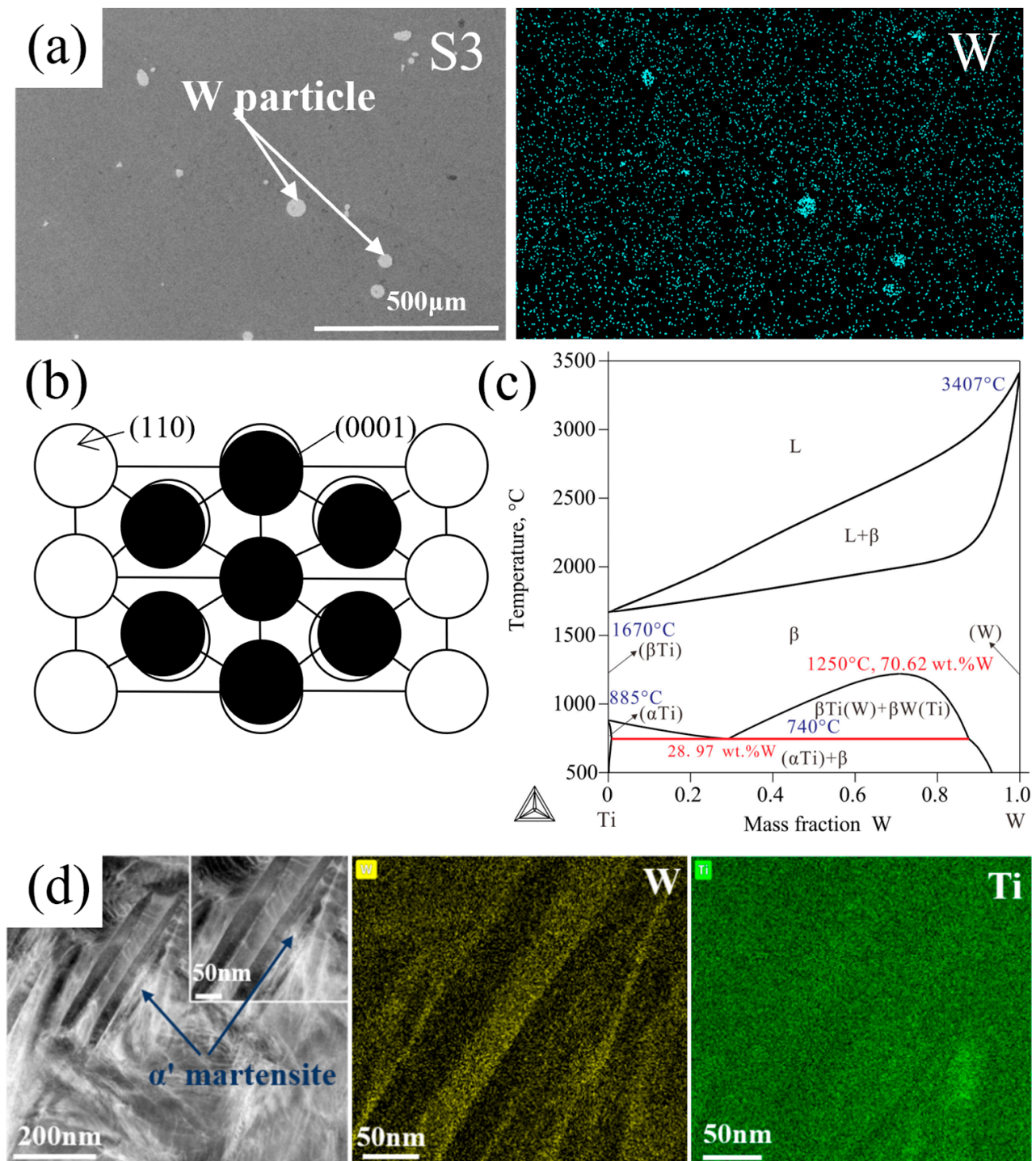


Figure 4. Elemental distribution of the S3 alloy: (a) SEM-EDS maps reveals the distribution of W; (b) Schematic diagram of the conversion of α -Ti to β -Ti; (c) Tungsten–Titanium Phase Diagram [23]; (d) High-angle annular dark-field phase of S3 sample and its partial magnified image, and the distribution of tungsten and titanium elements in the magnified image.

As shown in the SEM-EDS maps image of sample S3 in Figure 4a, the tungsten is distributed throughout the matrix. This indicates that tungsten is fully diffused inside the titanium matrix. As shown in Figure 4b, it may be that when the α -Ti of hcp crystal structure is transformed into the β -Ti of bcc structure, the base plane (0001) of hcp- α is transformed into the most densely arranged plane (110) in the bcc- β phase, the interplanar crystal spacing of the (110) face in the β phase will be slightly smaller than that of the

corresponding face (0001) in the α phase, which makes the stacking of titanium atoms loose and thus generates many vacant sites. At the same time, the atomic radius of tungsten atoms is close to that of titanium. Therefore, tungsten atoms can diffuse rapidly in bcc- β Ti with vacancies and diffuse uniformly through the whole titanium layer with a large diffusion rate. As mentioned above, although the melt pool duration is short, a significant amount of tungsten melts and diffuses completely into the titanium matrix due to thermal cycling and the large diffusion rate of tungsten into titanium as well as the infinite solid solution between tungsten and titanium. Tungsten is less distributed in the α' martensite and more distributed in the β phase matrix (Figure 4d). According to the W-Ti phase diagram (Figure 4c) and Hume–Rothery rule, W has a low solubility in α' martensite, while it has a faster diffusion rate and higher solubility in β -Ti.

EDS-spot scan was performed on five different regions of the S1–S4 sample melt pool to estimate the mass percentage of tungsten solid solution in the matrix for different samples, and the results were averaged and listed in Table 1. The solid solution tungsten content in the titanium matrix of S1–S4 samples gradually increased with the addition of tungsten, indicating that the amount of tungsten–titanium solid solution produced in the samples gradually increased with the addition of tungsten and was not yet saturated.

Table 1. The average EDS-spot scan of tungsten content in five regions for each sample in S1–S4.

Sample	S1	S2	S3	S4
Average W content (at%)	1.09%	1.83%	2.99%	4.94%

In order to further confirm the microstructure of the titanium alloy after the addition of tungsten, TEM analysis was performed on the S3 sample. As shown in the TEM bright-field images of Figure 5a, the microscopic morphology of the sample consists of needle-like α' martensite and tungsten–titanium solid solution matrix. The large range of needle-like α' martensite in Figure 5a is mostly less than 1 μm , indicating that the addition of tungsten plays a very effective role in grain refinement of α' martensite. As expected, α' martensite is surrounded by a large number of entangled dislocations. These dislocations provide part of the driving force during α' martensite nucleation and growth and promote the generation of α' cluster structures. The selected area electron diffraction (SAED) patterns in Figure 5c define the structure of the needle-like α' martensite. Higher magnification images of the α' martensite are shown in Figure 5d. In the mutually perpendicular α' martensite of Figure 5d, the lattice spacing is measured to be 0.25 nm, corresponding to the (10 $\bar{1}$ 0) crystal plane of α' martensite.

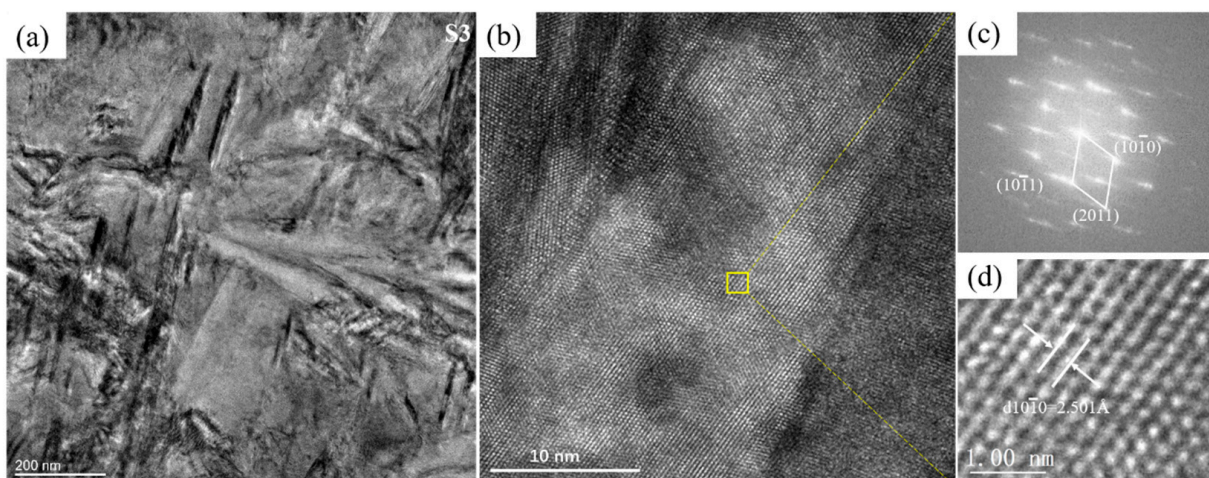


Figure 5. TEM bright-field images of S3 sample: (a,b) showing the martensite features of the Ti6Al4V-W samples; (c) SAED patterns corresponding to the rectangle parts in (b); (d) enlarged views of the rectangle parts in (b).

3.3. Mechanical Performance of Additive Manufacturing Ti6Al4V-W

Figure 6a shows the tensile properties of the Ti6Al4V-W alloys. The ultimate tensile strength (UTS) and yield strength (YS) increase greatly with increasing W content until the strengthening effect of the S4 sample reaches saturation and the strength decreases instead. Compared with the Ti6Al4V deposit, the strengthening effect peaks at sample S3, which are 1333 MPa and 1219 MPa for UTS and YS, respectively. Compared with the UTS and YS of S0 (Ti6Al4V) samples, which are 940 MPa and 860 MPa, respectively. The tungsten-added tungsten samples both increased about 42%.

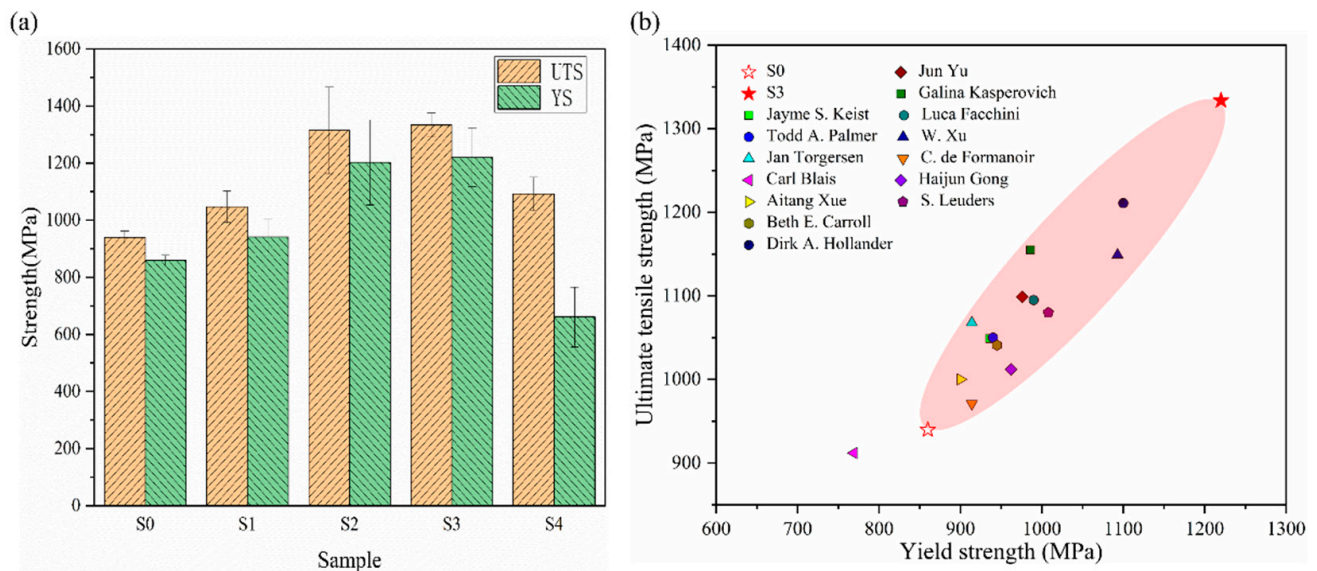


Figure 6. (a) The tensile properties of Ti6Al4V-W deposits, and (b) ultimate tensile strength versus yield strength of the as-printed Ti6Al4V-W alloy as compared with Ti6Al4V alloy produced by additive manufacturing methods [8,12,13,24–34].

Based on the available tensile property data of Ti6Al4V in the literature [8,12,13,24–34], in Figure 6b we compare the tensile strength of Ti6Al4V produced by different additive manufacturing techniques. The comparison shows that the addition of W to Ti6Al4V does have a large enhancement effect on the mechanical properties of Ti6Al4V.

The increase in strength arises from two aspects: one is the grain refinement enhancement effect caused by the reduction of β grain and α' martensite size; the other is the solid solution strengthening effect caused by the formation of replacement solid solution between tungsten and titanium.

3.3.1. Grain Refinement Effect

According to the Hall–Petch effect, grain refinement can effectively enhance the strength of the sample. On the other hand, the thinning of the α' martensite width also leads to an increase in strength [35]. We counted the size (length and width) of α' martensite in some areas of each sample and produced histograms of the distribution of the sizes and the average values (Figure 7). The α' martensite of S4 is close to disappearing, so it failed to be counted. With the addition of tungsten, the length and width of α' martensite were greatly reduced, and the average length and width were refined from 2.38 μm and 480.24 nm, respectively, for sample S0 without initial tungsten addition to 310 nm and 61 nm, respectively, for sample S3. The average length and width of the α -laths both are reduced by about 87%, when compared with the α -laths of Ti6Al4V deposit. This shows how significant the effect of the addition of W is on the grain refinement of TC4.

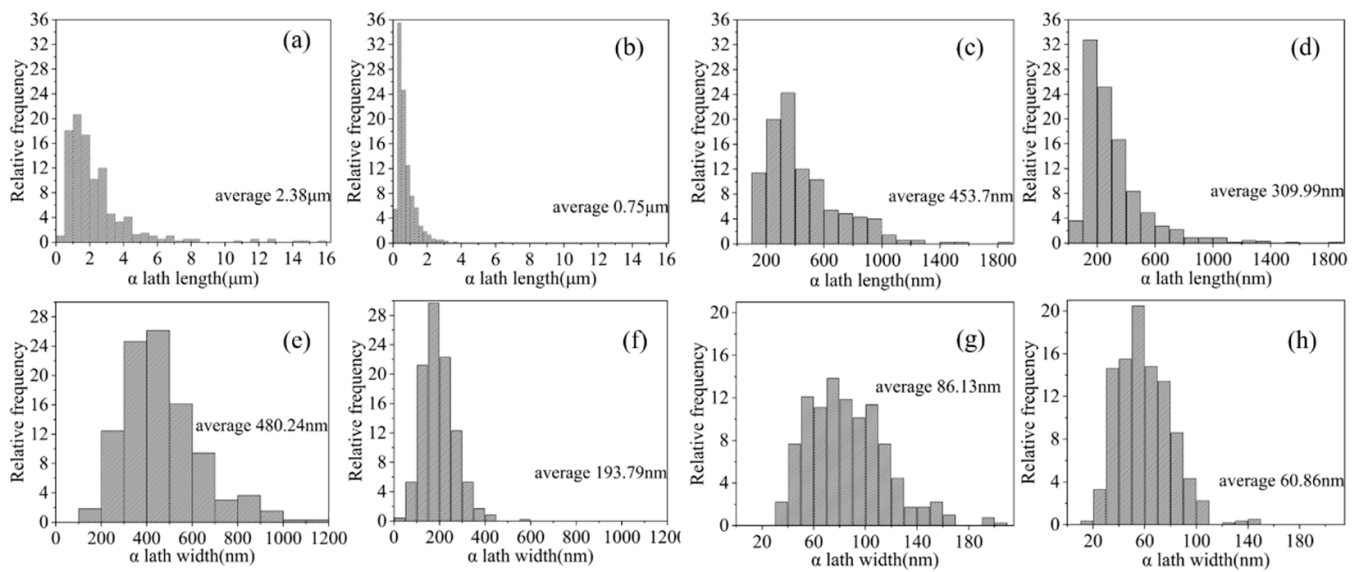


Figure 7. The sizes of the α -laths in Ti6Al4V-W deposits: (a,e) S0; (b,f) S1; (c,g) S2; (d,h) S3.

According to the Easton and St. John model, the larger the Q value of the element on the titanium alloy grain refinement the stronger the effect is. The W element on the titanium alloy growth limiting factor Q value has 22C0, and the titanium alloy grain refining element is also considered quite large. Therefore, the addition of tungsten at the solid–liquid solidification front can add more structural subcooling and grain refinement increases with increasing solute content until the saturation point is reached. This reason explains well the significant refinement of the prior- β grains with increasing tungsten content.

In addition, as mentioned in Figure 8b, T_l and T_r are the α' martensite transformation temperature in the region with less tungsten and rich tungsten, respectively. As show in Figure 8a, when the temperature exceeds the T_l but is lower than the solidification temperature, the solidification will produce areas containing alternating different components due to dendrite segregation. As the temperature gradually decreases, when the temperature is between T_r and T_l , the part with less tungsten content starts to generate α' martensite first, and the region with higher tungsten content is still mainly composed of β -Ti, which hinders the growth of α' martensite in the region with less tungsten content. Hence, the growth of α' martensite in this part is only possible in a relatively narrow region (about 2 μm), thus refining the α' martensite in this region. With a further decrease of the temperature, when the temperature is less than T_r , the transformation of the α' martensite in the region with higher tungsten content also takes place. On the one hand, the α' martensite in the region with less tungsten content has previously formed, which prevents the growth of new α' martensite, and on the other hand more β -crystals are retained in the region with higher content of β -stabilizing elements of tungsten thus preventing the transformation of the β phase into α' martensite, so fewer regions of α' martensite can grow and thus refine the α' martensite.

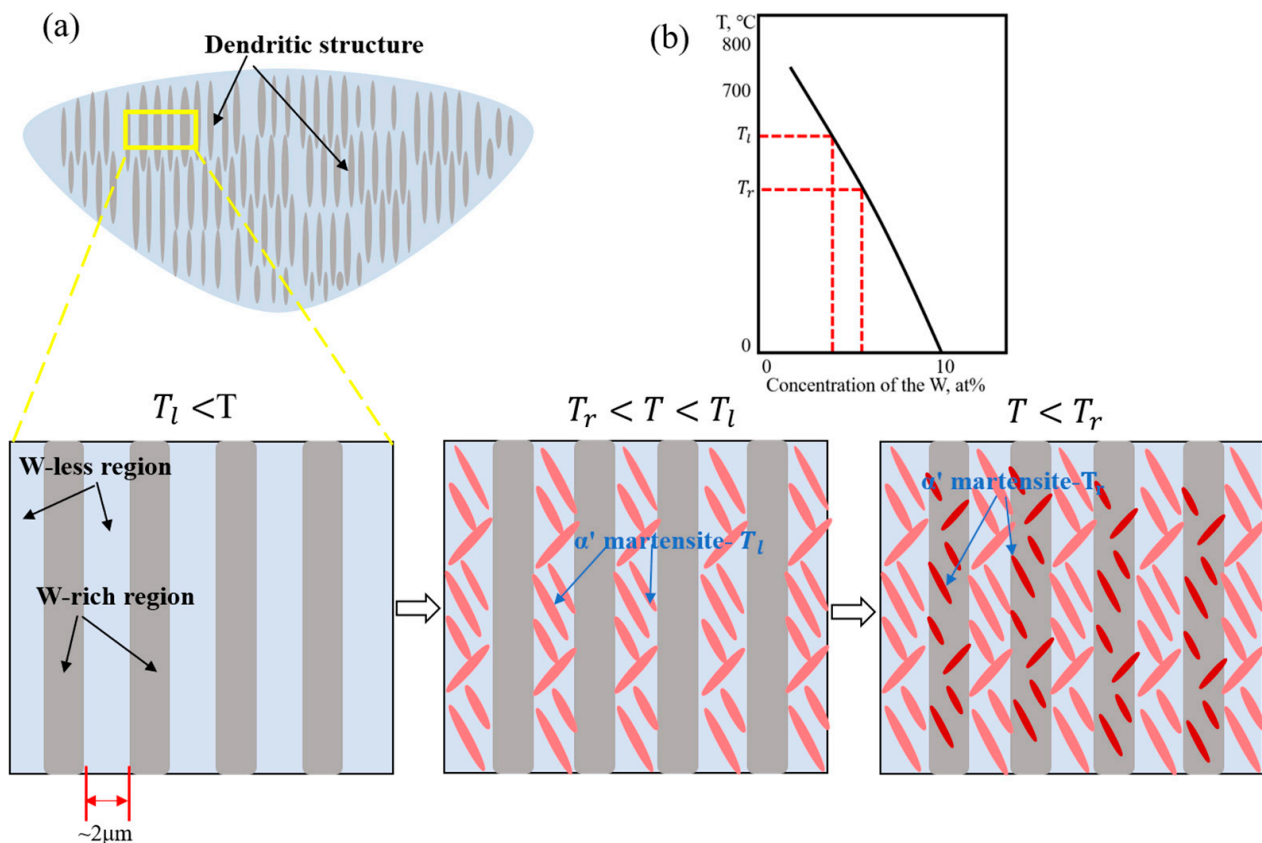


Figure 8. (a) Schematic diagram of α' martensite formation during solidification, where light blue is the area with less tungsten, gray is the area with more tungsten, and red is α' martensite. (b) The martensitic transformation temperature of titanium as a function of alloying additions for W [36].

3.3.2. Other Effects

The solid solution strengthening theory shows that as the solid solution content in the sample increases, the strength of the sample also increases. However, if the solid solution content increases to a certain value, too much brittle phase in the sample deteriorates the mechanical properties of the material, so the strength of S4 decreases instead.

In order to measure the unmelted tungsten content in the sample, we performed an inductively coupled plasma (ICP) emission spectrometry test on the sample, as shown in Table 2. Compared with Table 1, the unmelted tungsten mass percentage difference is less, and converted to volume percentage is even less, so the unmelted tungsten has limited effect on the mechanical properties of the matrix.

Table 2. The ICP of tungsten content for each sample in S1–S4.

Sample	S1	S2	S3	S4
W content (at%)	1.40%	2.76%	3.09%	4.96%

4. Conclusions

In this study, we mixed a certain amount of tungsten powder with Ti6Al4V powder and printed high-strength titanium alloy samples containing unmelted tungsten particles. Next, we investigated the effects on the microstructure and tensile properties of the alloy samples and we provided a new method for preparing high-strength titanium alloys. The following are the main conclusions we reached:

(1) A Ti6Al4V-W alloy with great mechanical properties was successfully prepared by direct energy deposition. With the increase of tungsten, the amount of α' martensite decreased but became finer, the size of the β phase decreased and tended to be equiaxed.

Inside the melt pool, tungsten produced a strip-like dendrite due to its undercooling effect on titanium composition and its stabilizing effect on β -Ti.

(2) As the tungsten content increased, the ultimate tensile strength and yield strength of the samples also increased. The S3 sample showed a peak strengthening effect, with an ultimate tensile strength value of 1333 MPa and a yield strength value of 1219 MPa. Compared with the S0 (Ti6Al4V), which had ultimate tensile and yield strengths of 940 MPa and 860 MPa, respectively, the strength increased by 42%. This high strengthening effect is mainly due to the significant grain refinement in α' martensite and β phase caused by the addition of tungsten, as well as lattice distortion caused by the substitutional solid solution formed by tungsten and titanium.

Author Contributions: Conceptualization, J.X. and J.L.; formal analysis, J.X. and Y.S.; methodology, J.X. and J.L.; supervision, Y.S. and J.L.; writing—original draft preparation, J.X. and Y.S.; review and editing, Y.S. and Q.W. All authors have read and agreed to the published version of the manuscript.

Funding: This research was funded by the National Natural Science Foundation (No. 51932006), the National Key R&D Program of China (No. 2021YFB3802300), the Independent Innovation Projects of the Hubei Longzhong Laboratory (No. 2022ZZ-33), and the National Natural Science Foundation (No. 52104363).

Data Availability Statement: Data are not available.

Conflicts of Interest: The authors declare that they have no known competing financial interest or personal relationships that could appear to influence the work reported in this paper.

References

1. Zhang, T.; Liu, C.-T. Design of titanium alloys by additive manufacturing: A critical review. *Adv. Powder Mater.* **2022**, *1*, 100014. [[CrossRef](#)]
2. Kalashnikov, K.N.; Chumaevskii, A.V.; Kalashnikova, T.A.; Kolubaev, E.A. A substrate material and thickness influence on the 3D-printing of Ti-6Al-4V components via wire-feed electron beam additive manufacturing. *J. Mater. Res. Technol.* **2022**, *16*, 840–852. [[CrossRef](#)]
3. Gao, Z.; Shi, H.; Yang, X.; Lyu, F.; Wang, L.; Zhan, X. Influence of heat accumulation on the distribution uniformity of microstructure and mechanical properties of laser additive manufacturing joint of 80 mm thick Ti6Al4V titanium alloy plates. *J. Mater. Process. Technol.* **2022**, *310*, 117774. [[CrossRef](#)]
4. Dziaduszevska, M.; Zieliński, A. Structural and Material Determinants Influencing the Behavior of Porous Ti and Its Alloys Made by Additive Manufacturing Techniques for Biomedical Applications. *Materials* **2021**, *14*, 712. [[CrossRef](#)] [[PubMed](#)]
5. Promopatum, P.; Yao, S.-C. Influence of scanning length and energy input on residual stress reduction in metal additive manufacturing: Numerical and experimental studies. *J. Manuf. Process.* **2020**, *49*, 247–259. [[CrossRef](#)]
6. Choi, Y.R.; Sun, S.D.; Liu, Q.; Brandt, M.; Qian, M. Influence of deposition strategy on the microstructure and fatigue properties of laser metal deposited Ti-6Al-4V powder on Ti-6Al-4V substrate. *Int. J. Fatigue* **2020**, *130*, 105236. [[CrossRef](#)]
7. Brika, S.E.; Letenneur, M.; Dion, C.A.; Brailovski, V. Influence of particle morphology and size distribution on the powder flowability and laser powder bed fusion manufacturability of Ti-6Al-4V alloy. *Addit. Manuf.* **2020**, *31*, 100929. [[CrossRef](#)]
8. Keist, J.S.; Palmer, T.A. Role of geometry on properties of additively manufactured Ti-6Al-4V structures fabricated using laser based directed energy deposition. *Mater. Des.* **2016**, *106*, 482–494. [[CrossRef](#)]
9. Zhang, T.; Huang, Z.; Yang, T.; Kong, H.; Luan, J.; Wang, A.; Wang, D.; Kuo, W.; Wang, Y.; Liu, C.T. In situ design of advanced titanium alloy with concentration modulations by additive manufacturing. *Science* **2021**, *374*, 478–482. [[CrossRef](#)]
10. Gou, J.; Wang, Z.; Hu, S.; Shen, J.; Tian, Y.; Zhao, G.; Chen, Y. Effects of trace Nb addition on microstructure and properties of Ti-6Al-4V thin-wall structure prepared via cold metal transfer additive manufacturing. *J. Alloys Compd.* **2020**, *829*, 154481. [[CrossRef](#)]
11. Avila, J.D.; Alrawahi, Z.; Bose, S.; Bandyopadhyay, A. Additively Manufactured Ti6Al4V-Si-Hydroxyapatite composites for articulating surfaces of load-bearing implants. *Addit. Manuf.* **2020**, *34*, 101241. [[CrossRef](#)] [[PubMed](#)]
12. Xue, A.; Lin, X.; Wang, L.; Wang, J.; Huang, W. Influence of trace boron addition on microstructure, tensile properties and their anisotropy of Ti6Al4V fabricated by laser directed energy deposition. *Mater. Des.* **2019**, *181*, 107943. [[CrossRef](#)]
13. Rousseau, J.N.; Bois-Brochu, A.; Blais, C. Effect of oxygen content in new and reused powder on microstructural and mechanical properties of Ti6Al4V parts produced by directed energy deposition. *Addit. Manuf.* **2018**, *23*, 197–205. [[CrossRef](#)]
14. Mendoza, M.Y.; Samimi, P.; Brice, D.A.; Martin, B.W.; Rolchigo, M.R.; LeSar, R.; Collins, P.C. Microstructures and Grain Refinement of Additive-Manufactured Ti-xW Alloys. *Metall. Mater. Trans. A* **2017**, *48*, 3594–3605. [[CrossRef](#)]
15. Bermingham, M.J.; McDonald, S.D.; StJohn, D.H.; Dargusch, M.S. Beryllium as a grain refiner in titanium alloys. *J. Alloys Compd.* **2009**, *481*, L20–L23. [[CrossRef](#)]

16. Easton, M.A.; StJohn, D.H. The Effect of Alloy Content on the Grain Refinement of Aluminium Alloys. In *Essential Readings in Light Metals*; Grandfield, J.F., Eskin, D.G., Eds.; Springer International Publishing: Cham, Switzerland, 2016; pp. 393–399.
17. Xu, Y.; Fu, Y.; Li, J.; Xiao, W.; Zhao, X.; Ma, C. Effects of tungsten addition on the microstructural stability and properties of Ti-6.5Al-2Sn-4Hf-2Nb-based high temperature titanium alloys. *J. Mater. Sci. Technol.* **2021**, *93*, 147–156. [[CrossRef](#)]
18. Zhang, W.J.; Song, X.Y.; Hui, S.X.; Ye, W.J.; Wang, Y.L.; Wang, W.Q. Tensile behavior at 700 °C in Ti–Al–Sn–Zr–Mo–Nb–W–Si alloy with a bi-modal microstructure. *Mater. Sci. Eng. A* **2014**, *595*, 159–164. [[CrossRef](#)]
19. Gu, D.; Shen, Y. Balling phenomena in direct laser sintering of stainless steel powder: Metallurgical mechanisms and control methods. *Mater. Des.* **2009**, *30*, 2903–2910. [[CrossRef](#)]
20. Rolchigo, M.R.; Mendoza, M.Y.; Samimi, P.; Brice, D.A.; Martin, B.; Collins, P.C.; LeSar, R. Modeling of Ti-W Solidification Microstructures Under Additive Manufacturing Conditions. *Metall. Mater. Trans. A* **2017**, *48*, 3606–3622. [[CrossRef](#)]
21. Ahmed, T.; Rack, H.J. Phase transformations during cooling in $\alpha+\beta$ titanium alloys. *Mater. Sci. Eng. A* **1998**, *243*, 206–211. [[CrossRef](#)]
22. Qian, L.; Mei, J.; Liang, J.; Wu, X. Influence of position and laser power on thermal history and microstructure of direct laser fabricated Ti-6Al-4V samples. *Mater. Sci. Technol.* **2013**, *21*, 597–605. [[CrossRef](#)]
23. Huang, L.; Zhang, J.; Pan, Y.; Du, Y. Spark plasma sintering of W-10Ti high-purity sputtering target: Densification mechanism and microstructure evolution. *Int. J. Refract. Met. Hard Mater.* **2020**, *92*, 105313. [[CrossRef](#)]
24. Hollander, D.A.; von Walter, M.; Wirtz, T.; Sellei, R.; Schmidt-Rohlfing, B.; Paar, O.; Erli, H.J. Structural, mechanical and in vitro characterization of individually structured Ti-6Al-4V produced by direct laser forming. *Biomaterials* **2006**, *27*, 955–963. [[CrossRef](#)]
25. Facchini, L.; Magalini, E.; Robotti, P.; Molinari, A.; Höges, S.; Wissenbach, K. Ductility of a Ti-6Al-4V alloy produced by selective laser melting of prealloyed powders. *Rapid. Prototyp. J.* **2010**, *16*, 450–459. [[CrossRef](#)]
26. Yu, J.; Rombouts, M.; Maes, G.; Motmans, F. Material Properties of Ti6Al4V Parts Produced by Laser Metal Deposition. *Physcs. Proc.* **2012**, *39*, 416–424. [[CrossRef](#)]
27. Leuders, S.; Thöne, M.; Riemer, A.; Niendorf, T.; Tröster, T.; Richard, H.A.; Maier, H.J. On the mechanical behaviour of titanium alloy TiAl6V4 manufactured by selective laser melting: Fatigue resistance and crack growth performance. *Int. J. Fatigue* **2013**, *48*, 300–307. [[CrossRef](#)]
28. Carroll, B.E.; Palmer, T.A.; Beese, A.M. Anisotropic tensile behavior of Ti-6Al-4V components fabricated with directed energy deposition additive manufacturing. *Acta Mater.* **2015**, *87*, 309–320. [[CrossRef](#)]
29. Gong, H.; Rafi, K.; Gu, H.; Janaki Ram, G.D.; Starr, T.; Stucker, B. Influence of defects on mechanical properties of Ti-6Al-4V components produced by selective laser melting and electron beam melting. *Mater. Des.* **2015**, *86*, 545–554. [[CrossRef](#)]
30. Kasperovich, G.; Hausmann, J. Improvement of fatigue resistance and ductility of TiAl6V4 processed by selective laser melting. *J. Mater. Process. Technol.* **2015**, *220*, 202–214. [[CrossRef](#)]
31. Keist, J.S.; Palmer, T.A. Development of strength-hardness relationships in additively manufactured titanium alloys. *Mater. Sci. Eng. A* **2017**, *693*, 214–224. [[CrossRef](#)]
32. Xu, W.; Lui, E.W.; Pateras, A.; Qian, M.; Brandt, M. In situ tailoring microstructure in additively manufactured Ti-6Al-4V for superior mechanical performance. *Acta Mater.* **2017**, *125*, 390–400. [[CrossRef](#)]
33. Razavi, S.M.J.; Bordonaro, G.G.; Ferro, P.; Torgersen, J.; Berto, F. Fatigue Behavior of Porous Ti-6Al-4V Made by Laser-Engineered Net Shaping. *Materials* **2018**, *11*, 284. [[CrossRef](#)]
34. de Formanoir, C.; Martin, G.; Prima, F.; Allain, S.Y.P.; Dessolier, T.; Sun, F.; Vivès, S.; Hary, B.; Bréchet, Y.; Godet, S. Micromechanical behavior and thermal stability of a dual-phase $\alpha+\alpha'$ titanium alloy produced by additive manufacturing. *Acta Mater.* **2019**, *162*, 149–162. [[CrossRef](#)]
35. Galarraga, H.; Warren, R.J.; Lados, D.A.; Dehoff, R.R.; Kirka, M.M.; Nandwana, P. Effects of heat treatments on microstructure and properties of Ti-6Al-4V ELI alloy fabricated by electron beam melting (EBM). *Mater. Sci. Eng. A* **2017**, *685*, 417–428. [[CrossRef](#)]
36. Dobromyslov, A.V.; Elkin, V.A. Martensitic transformation and metastable β -phase in binary titanium alloys with d-metals of 4–6 periods. *Scr. Mater.* **2001**, *44*, 905–910. [[CrossRef](#)]

Disclaimer/Publisher’s Note: The statements, opinions and data contained in all publications are solely those of the individual author(s) and contributor(s) and not of MDPI and/or the editor(s). MDPI and/or the editor(s) disclaim responsibility for any injury to people or property resulting from any ideas, methods, instructions or products referred to in the content.